

## SHORES II: Multi-frequency Characterisation of the Sub-mJy Radio Population in FIR-selected Fields

MERIEM BEHIRI <sup>1,2,3,4</sup> MARCELLA MASSARDI <sup>5,1</sup> VINCENZO GALLUZZI <sup>3,6</sup> MARIKA GIULIETTI <sup>3</sup>  
GAYATHRI GURURAJAN <sup>1,4</sup> ISABELLA PRANDONI <sup>3</sup> AND ANDREA LAPI <sup>1,3,4,7</sup>

<sup>1</sup>*Scuola Internazionale Superiore di Studi Avanzati, Via Bonomea 265, 34136 Trieste, Italy*

<sup>2</sup>*INAF-OAS Bologna, via Gobetti 101, I-40129 Bologna, Italy*

<sup>3</sup>*INAF - Istituto di Radioastronomia, Via Gobetti 101, 40129 Bologna, Italy*

<sup>4</sup>*Institute for Fundamental Physics of the Universe (IFPU), Via Beirut 2, 34014 Trieste*

<sup>5</sup>*INAF - Istituto di Radioastronomia - Italian ALMA Regional Centre, Via Gobetti 101, 40129 Bologna, Italy*

<sup>6</sup>*INAF-Osservatorio Astronomico di Trieste - Italian Astronomical Archives, via Tiepolo 11, 34131 Trieste, Italy*

<sup>7</sup>*Istituto Nazionale Fisica Nucleare (INFN), Sezione di Trieste, Via Valerio 2, 34127 Trieste, Italy*

### ABSTRACT

We present a new deep multi-frequency radio survey of two extragalactic fields observed with the Australia Telescope Compact Array (ATCA) as part of the SHORES project (Serendipitous H-ATLAS-fields Observations of Radio Extragalactic Sources). The observations, centred at 2.1, 5.5, and 9 GHz, cover the central 0.5 deg<sup>2</sup> of two Herschel Astrophysical Terahertz Large Area Survey (H-ATLAS) fields down to rms sensitivities of 9–17  $\mu$ Jy/beam at 2.1 GHz, 28–39  $\mu$ Jy/beam at 5.5 GHz and 38–61  $\mu$ Jy/beam at 9 GHz. This setup allows us to investigate the spectral energy distributions (SEDs) of faint radio sources and probe the nature of the sub-mJy population. We extract and validate a robust catalogue of 489 sources at 2.1 GHz, 101 of which are also detected at 5.5 GHz. We perform a multi-frequency analysis of the radio number counts and derive the spectral indices of sources in the deep fields. The spectral index distribution of our sources peaks around  $\alpha \sim -0.7$ , consistent with synchrotron emission from the faint radio population. The number counts at 2.1 GHz are consistent with previous deep surveys and theoretical models, and provide a lower limit on the star-forming galaxy population, which is expected to dominate the faint end. The 5.5 GHz data offer new, direct constraints on the sub-mJy radio sky at higher frequencies. By cross-matching with the H-ATLAS catalogue, we identify a sample of sources with far-infrared (FIR) counterparts and explore the far-infrared–radio correlation (FIRRC). The sources with  $q_{\text{FIR}} \geq 1.69$  exhibit radio spectral indices typical of star-forming galaxies. Furthermore, we identify a population of radio-only sources with similar indices that may correspond to high-redshift SFGs, lacking counterparts in the FIR survey due to its limited resolution and sensitivity.

**Keywords:** Extragalactic radio sources (508) — Radio source catalogs (1356) — Radio interferometry (1346) — Surveys (1671)

### 1. INTRODUCTION

Over the past decades, radio astronomy has become a cornerstone in the study of galaxy formation and evolution, providing insights into active galactic nuclei (AGN) activity across cosmic time. However, technical limitations—particularly in sensitivity and resolution—have historically limited the detection and identification of

star-forming galaxies (SFGs) in statistical radio studies. In fact, faint radio sources, including SFGs and radio-quiet AGN, trace the build-up of stellar mass and black hole growth, even in heavily dust-obscured environments where optical and UV diagnostics fail (e.g. [Talia et al. 2021](#); [Behiri et al. 2023](#); [Gentile et al. 2024](#)). As such, deep radio surveys reaching sub-mJy sensitivities (e.g. [Smith et al. 2021](#); [Best et al. 2023](#); [Whittam et al. 2022](#); [Hale et al. 2023](#)) are essential to constrain the cosmic

star formation history and to investigate the complex interplay between star formation and AGN feedback.

Radio emission from SFGs arises primarily from two physical processes tied to massive star formation: thermal free-free (bremsstrahlung) emission from ionised gas in HII regions and non-thermal synchrotron radiation from relativistic electrons accelerated in supernova remnants (e.g. Condon et al. 1992; Murphy et al. 2009). The balance between these two components varies with galaxy age and star formation efficiency, imprinting distinctive spectral energy distributions (SEDs) observable at radio wavelengths. In parallel, dust grains formed in the ejecta of massive stars absorb UV photons from young stellar populations and re-radiate in the far-infrared (FIR), linking FIR and radio emission through the well-known far-infrared–radio correlation (FIRRC; e.g. Helou et al. 1985; Condon et al. 1992; Yun et al. 2001; Bell 2003; Ivison et al. 2010a; Sargent et al. 2010; Giulietti et al. 2022). This correlation constitutes a powerful diagnostic of star formation, provided that contamination from AGN-related emission is carefully addressed.

AGN, especially in their radio-loud phase, contribute significantly to the radio sky through synchrotron radiation from relativistic jets and lobes. These structures are powered by the extraction of rotational energy from spinning supermassive black holes, mediated by magnetic fields (e.g. Blandford & Znajek 1977). The spectral properties of AGN-related radio emission depend on several factors, including jet power, age, environment, and viewing angle, and can differ significantly from those of SFGs. At GHz frequencies, compact flat-spectrum cores, steep-spectrum lobes, peaked flaring jetted components, and curved spectra due to synchrotron ageing or self-absorption are commonly observed (e.g. Massardi et al. 2011).

To disentangle these populations and build a comprehensive picture of radio source evolution, a multi-wavelength approach is essential, together with a combination of wide and deep observations. While wide-area shallow surveys at  $\sim$ GHz frequencies, such as RACS (McConnell et al. 2020), excel at detecting bright, extended radio sources, but they often lack the resolution or depth needed to characterise the faint, compact population of SFGs. Further, the MIGHTEE survey (Jarvis et al. 2016) provides wide-area deep radio imaging, complementary to the intermediate-depth, small-area observations presented here. On the other hand, higher-frequency observations—particularly in the 2–10 GHz range—offer higher resolution, probe rest-frame frequencies where thermal processes may become relevant. This spectral window captures the contribution

by both AGN and star-formation, making it particularly suitable to study faint galaxies and disentangle the physical processes that fuel the radio emission.

Within this context, we started the SHORES project (Serendipitous H-ATLAS-fields Observations of Radio Extragalactic Sources, Massardi et al. 2025), designed to exploit the synergy between deep radio observations and the rich far-infrared coverage provided by the Herschel Astrophysical Terahertz Large Area Survey (H-ATLAS; Eales et al. 2010). SHORES includes both shallow and deep fields, both surveyed at 2.1 GHz with the Australia Telescope Compact Array (ATCA), centred on a sample of candidate lensed galaxies in the South Galactic Pole (SGP) selected by Negrello et al. (2017) based on their FIR fluxes in H-ATLAS. This selection guarantees comprehensive FIR coverage across the observed fields. The shallow component, described in Massardi et al. (2025) (hereafter referred as SHORES-I), focused on the bright end of the 2.1 GHz radio population, dominated by AGN, and reached 95% completeness above 0.5 mJy over a 26 deg<sup>2</sup> surveyed area. Further, the deep fields have been also followed up at 5.5 and 9 GHz, to improve the radio photometric characterisation. In this paper, we present the analysis of the deep fields, which target the sub-mJy regime and are tailored to study the faint radio sources at 2.1, 5.5 and 9 GHz.

The deep observations reach rms sensitivities of 9–17  $\mu$ Jy/beam at 2.1 GHz and 28–39  $\mu$ Jy/beam at 5.5–9 GHz, over the two 0.5 deg<sup>2</sup> H-ATLAS fields. This allows robust source extraction, spectral index analysis, and cross-matching with FIR-selected galaxies. Combining radio and FIR data allows us to investigate the FIRRC down to faint flux levels, identify candidate high-redshift SFGs, and assess AGN contamination using spectral diagnostics.

This paper is structured as follows. In Section 2, we describe the observations, data reduction, and source extraction. Section 3 presents the multi-frequency catalogue and spectral index analysis. Section 5 focuses on the FIR cross-matching and the analysis of the FIRRC. In Section 6, we derive the radio number counts at 2.1 and 5.5 GHz. Finally, we discuss the implications of our results in Section 7.

Throughout this paper we define spectral indices  $\alpha$  so that flux densities scale as  $S_\nu \propto \nu^\alpha$ , and we adopt a flat  $\Lambda$ CDM cosmology (Planck Collaboration et al. 2020) with round parameter values  $h \approx 0.67$ ,  $\Omega_m \approx 0.3$  and  $\Omega_\Lambda \approx 0.7$ .

## 2. OBSERVATIONS AND DATA REDUCTION PROCESS FOR SHORES DEEP FIELDS

### 2.1. The deep fields selection

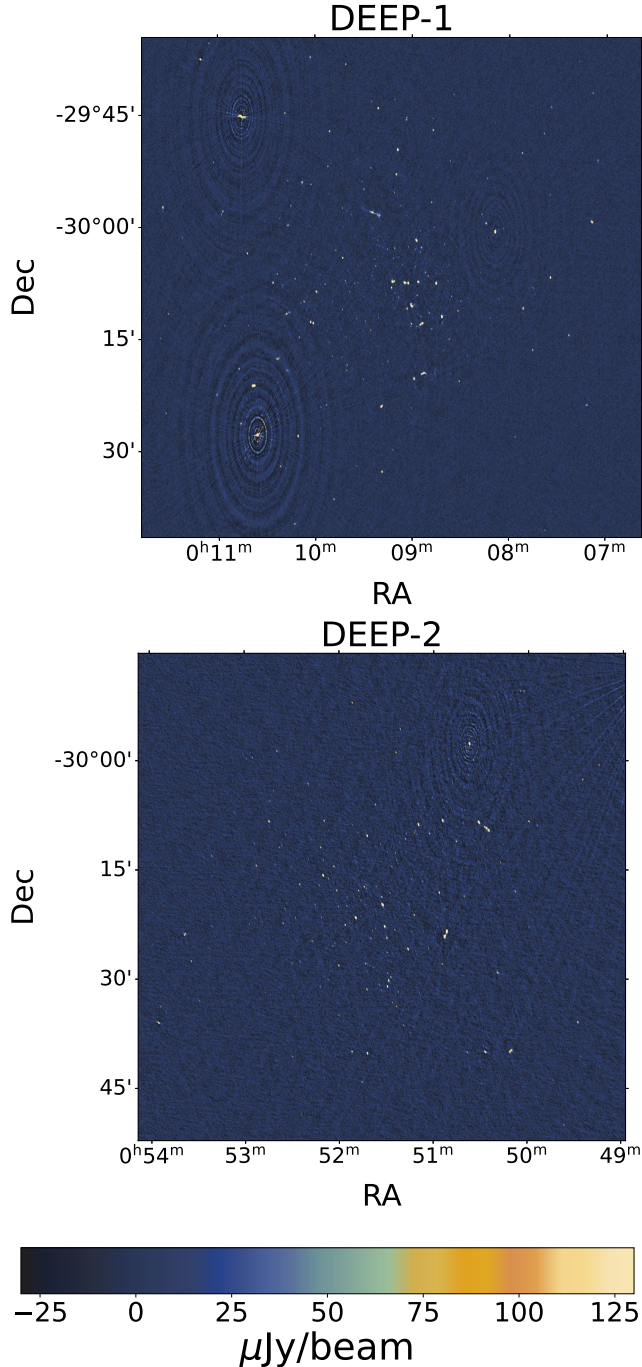


**Figure 1.** 2.1 GHz maps of the DEEP 1 (*top*) and DEEP 2 (*bottom*) fields. A single colour scale is shown below.

In the H/ATLAS SGP fields targeted by the SHORES survey, Negrello et al. (2017) identified 30 potential lensed sources. Among these, we identified the field at HATLASJ000912.7-300807 as notable due to its abundance of ancillary data. This particular field, especially its central lensed galaxy, had been previously observed with various instruments including the At-

**Table 1.** ATCA configurations and corresponding observing times for the SHORES deep fields

Date	Field	Band	Configuration
22OCT09	DEEP-1	4 cm	6D
22NOV29	DEEP-1,2	16 cm	6C
22NOV30	DEEP-1	16 cm	6C
22DEC20	DEEP-2	16 cm	6C
22DEC23	DEEP-1	4 cm	6C
22DEC29	DEEP-2	16 cm	6C
22DEC24	DEEP-1	16cm	6C
22DEC25	DEEP-1	16 cm	6C
22DEC27	DEEP-1	16 cm	6C
22DEC28	DEEP-1	4 cm	6C
22DEC29	DEEP-1	16 cm	6C
22DEC30	DEEP-1	16 cm	6C
23JEN26	DEEP-1	16 cm	6C
23DEC25	DEEP-1,2	16 cm	6D
24FEB29	DEEP-1	4 cm	6A
24MAR14	DEEP-1	4 cm	6A
24MAR18	DEEP-1,2	16 cm	6A
24APR28	DEEP-2	4 cm	6A
24MAY03	DEEP-2	4 cm	6A
24JUN09	DEEP-2	4 cm	6D

acama Large Millimeter Array (ALMA), the Hubble Space Telescope (HST), the Wide-field Infrared Survey Explorer (WISE), the GALaxy Evolution eXplorer (GALEX), the Kilo-Degree Survey (KiDS), and Spitzer surveys. Importantly, this field was free from interference by any extremely bright sources in radio surveys such as the NRAO VLA Sky Survey (NVSS) or the Rapid ASKAP Continuum Survey (RACS), which could affect our deeper observations. Hence, we selected it as the optimal candidate for more in-depth observations, naming it "DEEP-1".

The second deep field was selected combining two 2.1 GHz ATCA pointings centred to the lensed sources HATLASJ005132.8-01848 and HATLASJ005132.0-302011. These two fields happen to be closer than the 22.2 arcmin FWHM of the 2.1 GHz ATCA FoV, thus overlapping in FoV coverage. Therefore, we combined their observations to double the time on source for the area with respect to any other shallow field of the SHORES survey, building a "DEEP-2" field.

The two fields were observed in different epochs and with different calibrators; thus, they were reduced separately and consequently reached different sensitivity levels: extracted sources were combined in the analysis, accounting for the differences in the field maps where necessary, as described in the following section.

## 2.2. Observation, data reduction and imaging

In this section, we first describe the 2.1 GHz observations, which constitute the low-frequency component of the survey, and then the 5.5 and 9 GHz high-frequency observations.

### 2.2.1. 2.1 GHz observations

The low frequency observations span a 2 GHz bandwidth centered at 2.1 GHz and were run with the six 22-meter antennas of ATCA in the most extended E-W configurations and processed according to the procedures applied to all the other SHORES shallow fields, described in SHORES-I (see Tab. 1 of [Massardi et al. 2025](#) for the complete list of observing epochs, and a summary of it limited to the deep fields in Tab.1 below). PKS1934-638 was used as flux density and band-pass calibrator, and a set of bright sources (including PKS0008-421, PKS0008-264, PKS0118-272, PKS0426-380) were used as phase and polarization calibrators.

We also split the 2.1 GHz visibilities into four equally spaced sub-bands, centred at 1.3, 1.8, 2.3, and 2.9 GHz, and applied the same calibration and imaging procedures described in SHORES-I. This allowed us, where sensitivity permitted, to recover a more refined characterisation of the spectral behaviour of the detected sources, as discussed later in this paper.

### 2.2.2. 5.5 and 9 GHz observations

The central region ( $\sim 0.5 \text{ deg}^2$ ) of the deep fields was mapped in two Nyquist-sampled mosaics of 72 pointings each with the 4 cm receivers, configured with two simultaneous basebands centred at 5.5 and 9.0 GHz, respectively. Both the 5.5 and 9 GHz datasets were observed with a 2 GHz bandwidth. Observations were carried out with the ATCA over several nights between October 2022 and June 2024, as detailed in Table 1 (Projects C3502-CX542-C3605; PI: M. Behiri).

Calibration was performed according to standard procedures, using phase and polarisation calibrators such as PKS0023-263<sup>1</sup>, PKS2357-318, PKS0118-272, and PKS2337-334.

Maps of the calibrated data for each pointing were generated for each observed frequency and for the combined band (corresponding to a nominal frequency of 7.25 GHz) using the imaging software WSCLEAN ([Ofringa et al. 2014a](#)), similarly to what was done for the 2.1 GHz observations (SHORES-I). We adopt a robust (Briggs parameter set to 0.5) weighting scheme to strike

**Table 2.** Properties of the maps.

	Frequency [GHz]	Resolution [arcsec]	FOV	Area [deg <sup>2</sup> ]	Rms [μJy/beam]
DEEP-1	2.1	4.2×9.4	12.3′	1.25	9
	5.5	0.9×5.87	6.6′	0.6	39.1
	7.25	0.8×7.4	6.6′	0.6	28.5
	9.0	0.8×3.8	5.3′	0.43	37.9
DEEP-2	2.1	3.2×9.8	12.3′	1.25	18.2
	5.5	1.34×4.16	6.6′	0.6	55.3
	7.25	1.1×3.7	6.6′	0.6	39.5
	9.0	0.9×3.9	5.3′	0.43	60.1

*Notes* — Frequency: central (or effective) observing frequency of each map; <sup>†</sup> 7.25 GHz is the effective frequency of the multi-frequency synthesis (MFS) image combining the 5.5 and 9.0 GHz basebands. Resolution: synthesised beam FWHM. FOV: primary-beam FWHM of a single pointing at the given frequency. Area: total area of the map at that frequency. Rms: median image rms noise in the mosaic.

a balance between artefact suppression and the best sensitivity, and we exploit the auto-masking feature to identify all emissions above  $5\sigma$  significance level, hence perform a deep cleaning down to the noise level ( $1\sigma$ , autothreshold set to 1) over those regions.

We finally combine the various pointings to a mosaic for each field, exploiting the MIRIAD task LINMOS.

Both fields host sources brighter than expected at the selection stage, whose effect is not negligible at our final sensitivity level. In particular, DEEP-1 contains two sources with a peak flux density of  $\sim 2 \text{ mJy}$ . This generates an appreciable noise pattern in the maps. We exploited the bright source to apply a self-calibration procedure to reduce it. Therefore, at 2.1 GHz we reached an rms of  $\sim 9 \mu\text{Jy/beam}$  and of  $\sim 18.2 \mu\text{Jy/beam}$  respectively for the two fields.

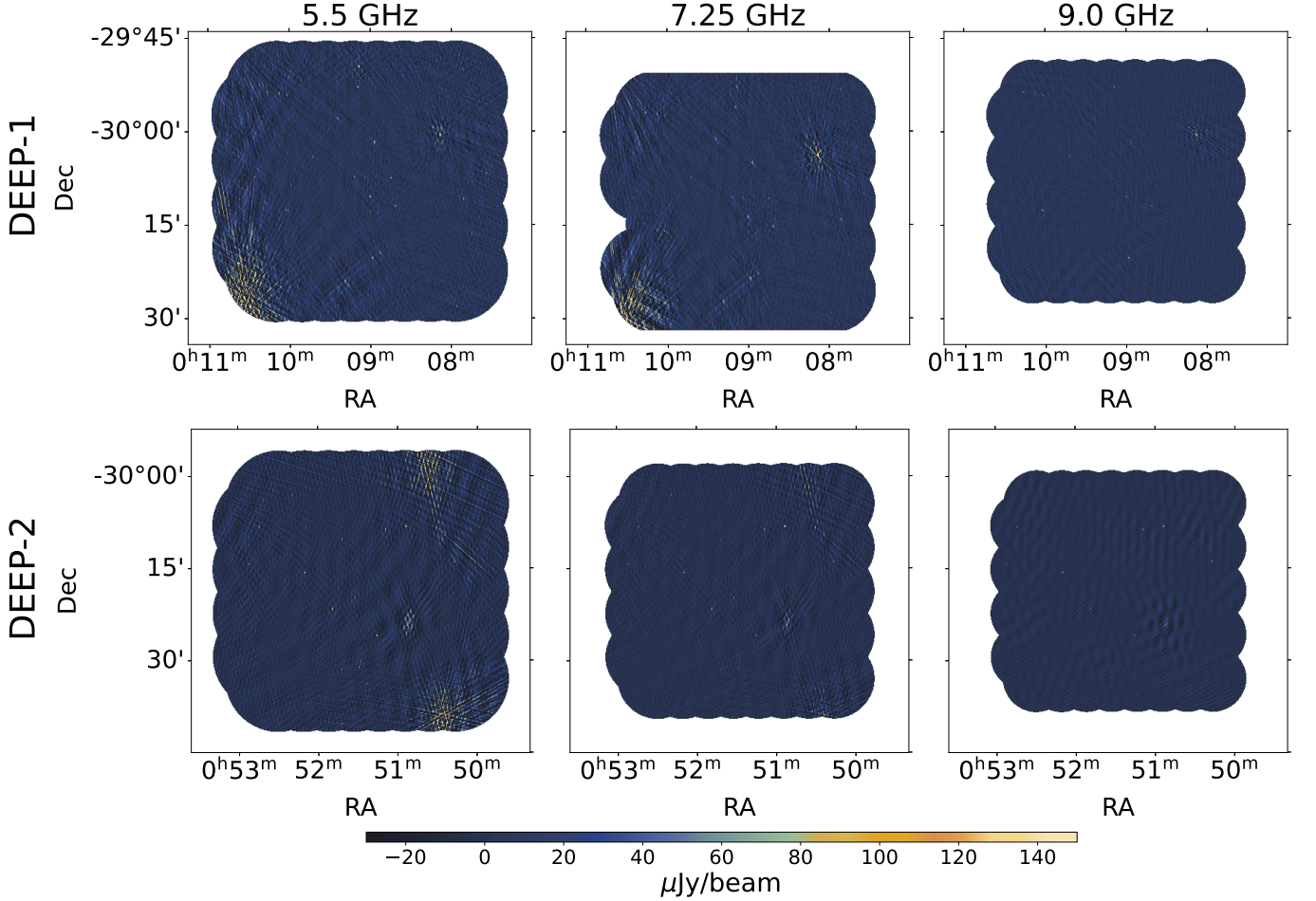
The same bright sources contaminating the 2.1 GHz maps happen to be at the edge of the mosaicked areas at 5.5 and 9.0 GHz (Figure 2). We identified the closest pointing and derived improved gain solutions to refine the calibration of any other pointings affected nearby. This allows us to reach a rather homogenous noise pattern in mosaicked maps.

Table 2 summarises the properties of the maps at all the reference frequencies.

Following the SHORES-I pipeline ([Massardi et al. 2025](#)), we use PYSE exclusively to generate rms maps, as it provides stable noise estimates across mosaics with spatially varying sensitivity. Source extraction is performed with BLOBCAT, which was shown in [Massardi et al. 2025](#) to be more suitable than PySE or Aegean in ATCA multi-pointing mosaics affected by residual side-lobes, given our purposes.

<sup>1</sup> Note that PKS0023-263 shows extended components at 9.0 GHz at our sensitivity; we accounted for this and also used additional calibrators.





**Figure 2.** Maps of the DEEP-1 (*top*) and DEEP-2 (*bottom*) at 5.5 (left), 7.25 (center), and 9.0 (right) GHz. Notice that the 7.25 GHz is the composed by multi-frequency synthesis of the other two frequencies, on which each 2 GHz baseband was centered.

Finally, Figure 3 illustrates the visibility region as a function of rms, i.e. the cumulative area of the maps where the local noise is below a given rms threshold. A slight shoulder in the PB-corrected curves is visible: in the single 2.1 GHz PB-corrected map the edges are noisier than the centre, so the effective-area curve can show a small bump (see also [Massardi et al. 2025](#)). This effect is also present in the mosaics, where changes in pointing overlap create rings with similar sensitivity, making the bump more noticeable at 5.5 GHz, where the mosaicked area is wider.

### 3. SOURCE EXTRACTION AND CATALOGUES

BLOBCAT ([Hales et al. 2012](#)) is based on the “flood-fill” algorithm and is specifically designed to perform efficient source extraction on radio survey data: we use it to identify candidate sources in the maps, following the procedure already tested in the SHORES shallow fields (SHORES-I).

At 2.1 GHz, we perform the detections on the non-primary beam-corrected maps. The primary beam correction is applied *a posteriori* using the polynomial form that was computed in SHORES-I which characterises the beam response out to the first null region. The MIRIAD task LINMOS used to combine the pointings into the 5.5–9.0 GHz mosaics applies the primary beam correction (pb-correction). Thus, the detection maps are already pb-corrected. In all the cases, we provide in input the rms maps produced by PYSE.

At 2.1 GHz, BLOBCAT extracts a total of 1480 sources above  $3\sigma$ , and 497 above  $4.5\sigma$ . Consistent with [Massardi et al. \(2025\)](#) and the standard practice adopted in radio surveys (e.g. [Franzen et al. 2015](#); [Smolčić et al. 2017](#); [Hancock et al. 2018](#); [Norris et al. 2021](#)), all  $4.5\text{--}5\sigma$  candidates were visually inspected to identify artefacts associated with ATCA sidelobes and non-Gaussian noise features. Detections were rejected only when showing clear sidelobe morphology, inconsistent centroiding, or placement in regions of unstable rms. This conservative

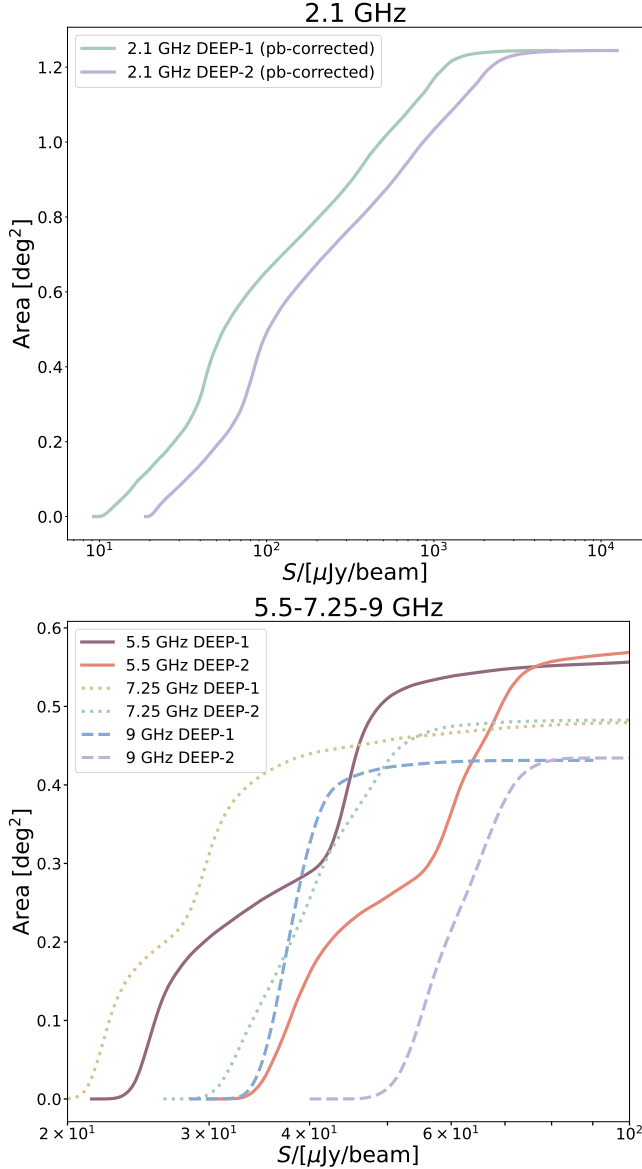


**Figure 3.** *Upper:* Effective area curves at 2.1 GHz (DEEP-1/DEEP-2), with primary-beam correction. *Lower:* Effective area at 5.5-7.25-9 GHz for DEEP-1 and DEEP-2.

step ensures a clean low-SNR catalogue while maintaining consistency with the formal false detection rate.

After visual inspection, we confirmed 483 genuine sources, including 16 composite objects, i.e. sources composed of multiple blobs that were initially detected as separate components.

We use the BLOBCAT-generated parameter  $R_{ext}$  to differentiate between unresolved and extended sources, classifying as extended those with  $R_{ext} > 1.4$ . This criterion ensures that in point sources the total-to-peak flux density ratio,  $S_T/S_P$ , is lower than 1.15 (Figure 4). As a result, at  $\text{SNR} > 4.5$  we get 429 point-like and 68 extended sources (including the composite ones).

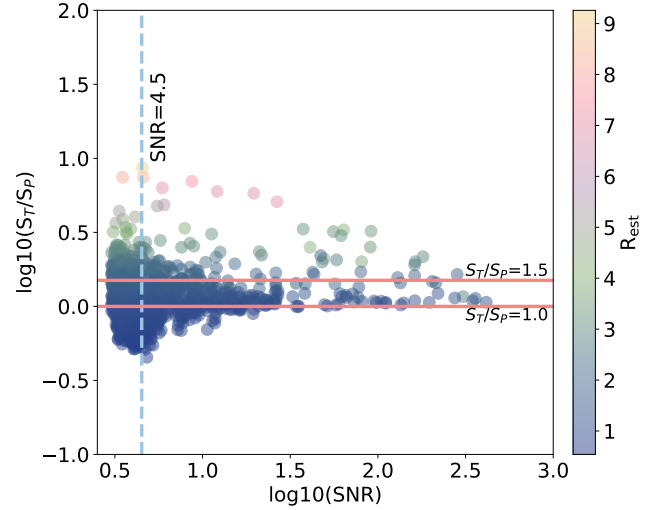


**Figure 4.** Ratio between total flux and peak flux as a function of the SNR for the SHORES sources.

To compute the reliability of the deep fields we changed the sign to the map pixel values to build the negative map of each field and extract the sources using BLOBCAT again. Thus, we estimate the False Detection Rate (FDR), i.e. the ratio between the detections on the negative maps (false detections) and the detections on the positive maps (real detections) at a given flux density level. We define the reliability as  $1 - \text{FDR}$ .

The reliability saturates at 1 when the number of false detections is null at a given flux density level, corresponding to a given SNR. For both the SHORES deep fields, we obtain a reliability of 95% at  $\text{SNR} \sim 5.0$  (Figure 5).

At  $\text{SNR} \sim 4.5$  the reliability is  $\sim 85\%$  for both fields. We use this threshold combined with the visual inspection, as was already done for the shallower fields (Massardi et al. 2025), to identify the sources that can be included in our catalogue and used for scientific analysis, if not stated differently (e.g. Section 6). We also verify the presence of counterparts at other wavelengths to strengthen the hypothesis that sources with  $4.5 < \text{SNR} < 5.0$  are also true (therefore, the catalogue reliability is indeed higher than 85%). The FDR quantifies the intrinsic statistical reliability, following the framework of Massardi et al. (2025). Cross-identifications do not modify the formal FDR but provide external support for the adopted selection of  $4.5\text{--}5\sigma$  detections, which are retained only after the quality checks described above.

To calculate our completeness we perform a 10,000 simulation placing a single point source with known flux

density in random positions across the negative maps using the MIRIAD task IMGEN, and calculate the percentage of input sources detected with BLOBCAT at a given flux density. A survey is 100% complete above a limiting flux  $S_{lim}$ , if it is possible to recover all the input sources with flux density  $S > S_{lim}$ . For the SHORES deep fields, we obtain 95% completeness at  $182.3 \mu\text{Jy}$  (SNR $\sim 20$ ) for DEEP-1 and at  $198.1 \mu\text{Jy}$  (SNR $\sim 10.9$ ) for DEEP-2.

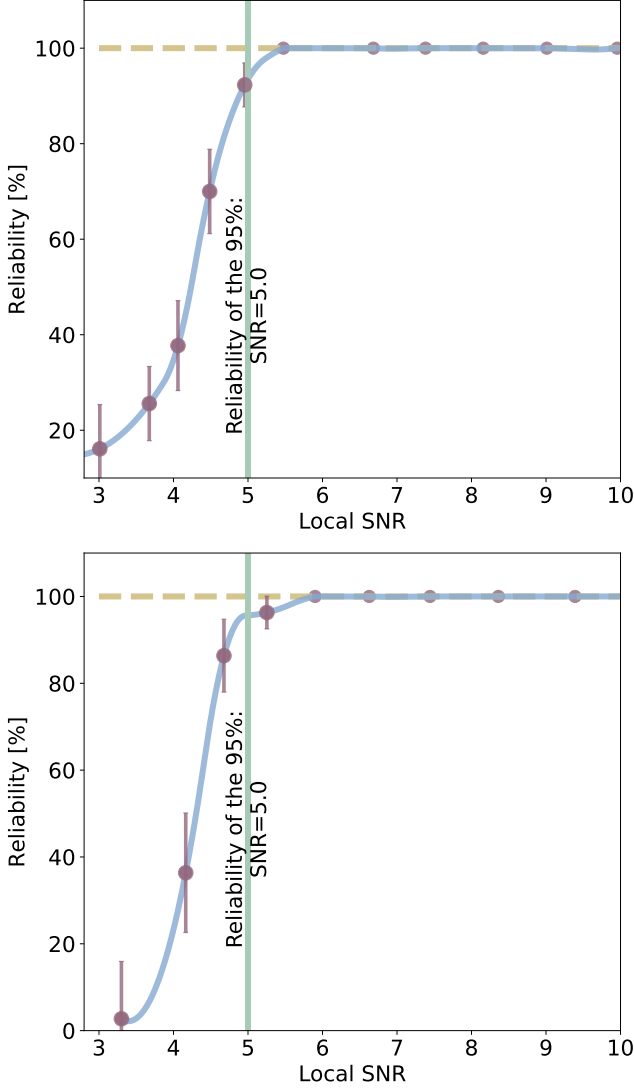


**Figure 5.** Reliability of the SHORES deep field (DEEP-1 on the top and DEEP-2 below) at 2.1 GHz. The green solid line indicates SNR = 5.08 (DEEP-1) and SNR = 5.00 (DEEP-2), for which the reliability is 95%.

Furthermore, we performed source extraction with BLOBCAT also on the maps of the 2.1 GHz sub-bands, corrected with the SHORES-I polynomial expression at the respective frequencies.

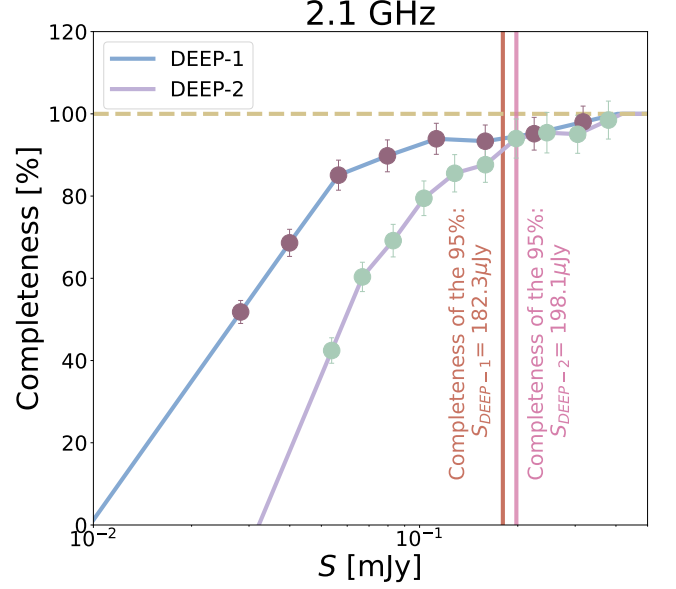


**Figure 6.** Completeness of the SHORES deep fields at 2.1 GHz. The solid vertical lines indicate the flux  $S$  at which the completeness is 95%.

Similarly to what was done at 2.1 GHz, we blindly extracted sources from the 5.5 GHz and 9 GHz mosaics, and from the combined 7.25 GHz map with BLOBCAT.

We perform a cross-match between the mosaics and the 2.1 GHz catalogues using a radius of  $3''$ , i.e. the lower limit of the resolution at 2.1 GHz, to identify counterparts.

After visual inspection, we obtain:

- At 5.5 GHz: 101 sources with SNR  $> 4.5\sigma$ , all of which have counterparts at 2.1 GHz. Among them, two are classified as composite sources.
- At 9.0 GHz: 33 sources with SNR  $> 4.5\sigma$ , all of which have counterparts at 2.1 GHz. Among them, one is classified as a composite source.
- In the composite 7.25 GHz map we detect 85 sources with SNR  $> 4.5\sigma$ , all matched at 2.1 GHz; none is composite. Notably, 29 of these are recovered *only* in the 7.25 GHz MFS image and not in the 5.5 and 9 GHz, i.e. at an even higher frequency, thanks to the improved sensitivity obtained by combining the two IFs (5.5 and 9.0 GHz).

We estimated the reliability and completeness of the mosaics, similarly to what is described in the previous sub-section (see Figure 7). The 95% reliability threshold at 5.5 GHz is reached at an SNR of approximately 5.1 for DEEP-1 and 5.0 for DEEP-2. At 9 GHz, the same reliability level is achieved at SNR = 4.8 for DEEP-1

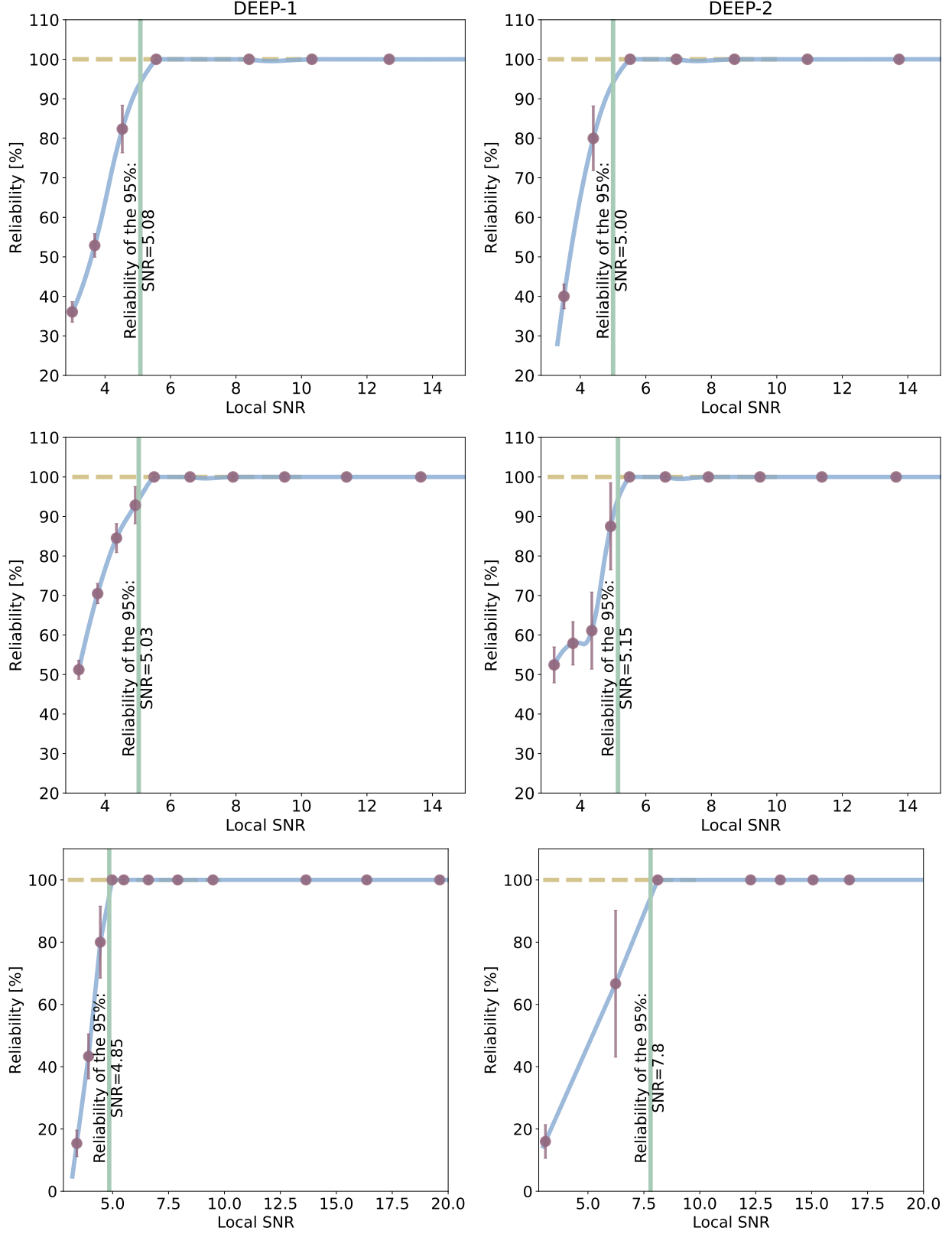


**Figure 7.** Reliability of the SHORES deep fields (DEEP-1 on the *left* and DEEP-2 on the *right*) at 5.5, 7.25 and 9.0 GHz. The green solid line indicates the SNR for which the reliability is 95%.



and 7.8 for DEEP-2. The worse performance of DEEP-2 at 9 GHz is driven by its less homogeneous  $uv$ -coverage (fewer integrations) compared to DEEP-1, which makes the mosaic less effective at mitigating pointing undersampling at this frequency (where the primary beam is smaller), resulting in a more structured noise pattern.

#### 4. RADIO SPECTRAL BEHAVIOUR

##### 4.1. Spectral behaviour in the SHORES bands

By matching the detections in our catalogues, we reconstructed the spectra of our sources across the 2.1–9.0 GHz range. Where sensitivity permitted (see Section 3), the 2.1 GHz sub-bands provided up to six frequency points to define the spectra. In addition, we used the 7.25 GHz composite MFS map to increase the likelihood of high-frequency counterparts for the faintest 2.1 GHz sources, as it reduces the noise of the 5.5 and 9.0 GHz maps by the expected factor of  $\sqrt{2}$ .

In total, we obtained 18 sources with only three spectral points at the main observed frequencies, and 96 sources with at least four points, of which 39 have six.

For all sources we used RADIOSED (Kerrison et al. 2024), a Bayesian radio SED-fitting tool that implements power-law, peaked, curved, and retriggered-AGN models to reconstruct the radio SED. We adopt the *low/high* convention:  $\alpha_{\text{low}}$  denotes the slope in the low-frequency branch *below* the spectral peak  $\nu_{\text{peak}}$  (typically attributed to the self-absorbed regime), while  $\alpha_{\text{high}}$  denotes the high-frequency slope *above*  $\nu_{\text{peak}}$  (usually considered optically thin).

The main SED parameters returned by the fitting (Fig. 8) are:

- $\nu_{\text{trough}}$ : the frequency of the SED minimum in the *retriggered* model; if present, the spectrum rises for  $\nu > \nu_{\text{trough}}$ .
- $\alpha_{\text{trough}}$ : the spectral index at  $\nu < \nu_{\text{trough}}$  (typically constrained by sub-GHz points in our sample).
- $\nu_{\text{peak}}$ : the frequency of the SED peak in *peaked/curved/retriggered* solutions.
- $\alpha_{\text{low}}$ : the spectral index across the low-frequency branch, i.e. for  $\nu_{\text{trough}} < \nu < \nu_{\text{peak}}$  (or, in the absence of a trough, immediately below  $\nu_{\text{peak}}$ ).
- $\alpha_{\text{high}}$ : the spectral index across the high-frequency branch, i.e. for  $\nu > \nu_{\text{peak}}$ .

To illustrate our convention, Fig. 8 shows three representative radio SEDs with their best-fitting models: a single power law, a peaked spectrum, and a retriggered spectrum. For clarity, we highlight in each model

the trough-frequency (trough), the low-frequency (low) and the high-frequency (high) branches of the model, corresponding to  $\alpha_{\text{low}}$  (below  $\nu_{\text{peak}}$ ) and  $\alpha_{\text{high}}$  (above  $\nu_{\text{peak}}$ ), and mark  $\nu_{\text{trough}}$  and  $\nu_{\text{peak}}$  where present. Here and throughout, the term *components* refers to the parametric branches of the fitted model, and should not be interpreted as necessarily distinct spatial emission regions.

As shown in the  $\alpha_{\text{high}} - \alpha_{\text{low}}$  radio colour-colour diagram in Figure 9, for the majority of sources (89 over 114) the best-fit model is a single power law, i.e.  $\alpha_{\text{high}} = \alpha_{\text{low}} \equiv \alpha_{\text{PL}}$ : 42.1% are classified as steep ( $\alpha_{\text{PL}} \leq -0.5$ ) and 33.3% as flat ( $|\alpha_{\text{PL}}| \lesssim 0.5$ ), while no truly inverted spectra ( $\alpha_{\text{PL}} > 0.5$ ) are found. Furthermore, the 18.4% exhibit peaked spectra, where  $\alpha_{\text{low}}$  and  $\alpha_{\text{high}}$  have opposite signs, indicating a clear turnover in the synchrotron SED. Two sources (1.8%) show curved but non-peaked spectra, suggestive of gentle curvature without a well-defined peak. Finally, 4.4% (5 objects) are best fit by the *retriggered* model, which describes spectra with a ‘valley’ followed by re-brightening: for these we use three indices— $\alpha_{\text{trough}}$  (before the minimum),  $\alpha_{\text{low}}$  (between the minimum and  $\nu_{\text{peak}}$ ), and  $\alpha_{\text{high}}$  (above  $\nu_{\text{peak}}$ ).

Compared to the analysis at higher flux densities in the same frequency regime by Galluzzi et al. (2017) (their Table 2), the fraction of steep-spectrum sources at SHORES depths appears slightly higher but still comparable (30% vs. our 34%).

Sources peaking above 2 GHz (i.e. those in the fourth quadrant of Fig. 9) are likely AGN-dominated, with emission enhanced by jetted components. In contrast, flat- and steep-spectrum sources comprise a mix of boosted quasar-like cores, optically thin lobe emission, and star-formation-related radio emission. Disentangling these contributions with  $\sim$ GHz data alone is challenging.

By plotting the distribution of spectral indices for flat- and steep-spectrum sources as a function of their 2.1 GHz flux density (Figure 10), we find that the two populations occupy distinct flux regimes. Steep-spectrum sources dominate at brighter flux densities, consistent with powerful AGN. This is partly due to selection effects: sources with rapidly declining spectra are harder to detect at high frequency, causing faint steep-spectrum sources to be under-represented.

Interestingly, the median spectral index flattens around  $\sim 1$  mJy before steepening again at lower fluxes. If observational bias were the only driver, a monotonic flattening with decreasing flux would be expected. The observed turnover instead points to a population transition: at intermediate fluxes, the emergence of flat-spectrum cores (e.g. low-luminosity AGN) flattens the

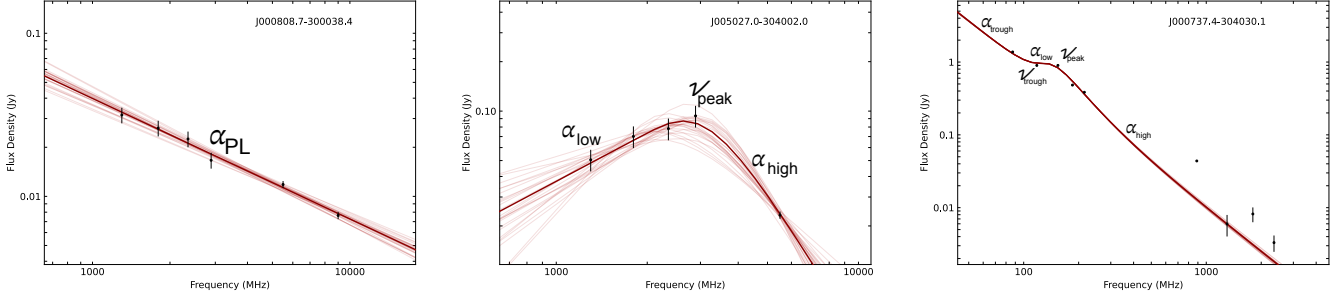


**Figure 8.** Example radio SEDs illustrating the fitted models and the *trough/low/high* convention. Points show the measured flux densities in the 0.1–10 GHz range. The best-fitting model is shown as a bright solid curve, with the different spectral index and frequency nomenclature highlighted by labels, accordingly. Shaded bands represent the 68% credible region from the RADIOSED posterior.

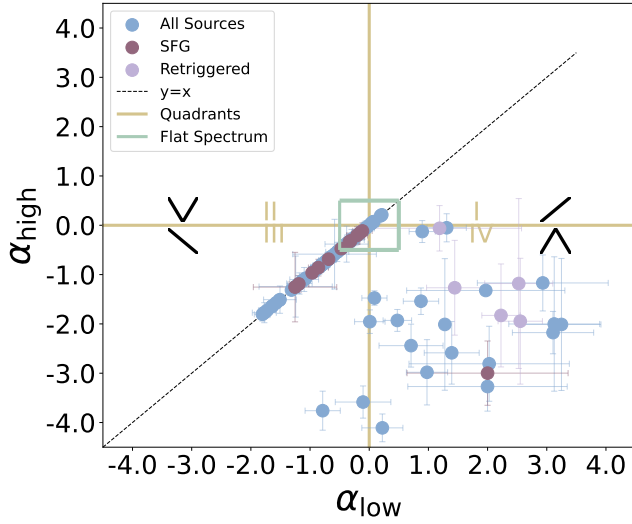


**Figure 9.** Colour-colour diagram of  $\alpha_{\text{low}}$  vs.  $\alpha_{\text{high}}$  from SHORES-only fits. SFGs (radio-normal) are identified via the FIR–radio correlation (Section 5): sources with  $q_{\text{FIR}} \geq 1.69$  (the lower  $1\sigma$  bound of the Ivison et al. 2010b relation, in our convention) are highlighted as maroon circles. Retriggered sources require an additional low-frequency index,  $\alpha_{\text{trough}}$ , defined below the SED minimum  $\nu_{\text{trough}}$ ; in this diagram we show  $(\alpha_{\text{low}}, \alpha_{\text{high}})$  measured for the post-minimum branch ( $\nu > \nu_{\text{trough}}$ ). Axes follow the low/high convention defined in Section 4.1. The green squared area indicates the locus of the flat-spectrum sources.

average spectral index, while at the faintest fluxes a steepening trend reappears, likely driven by starburst galaxies and possibly high-redshift AGN. These results align with similar behaviours reported in previous studies (e.g. Prandoni et al. 2006).

We emphasise that all flux densities were cross-checked for consistency across bands, and no evidence of calibration offsets was found that could artificially affect the observed spectral trends (see Massardi et al. 2025 and Section 4.2).

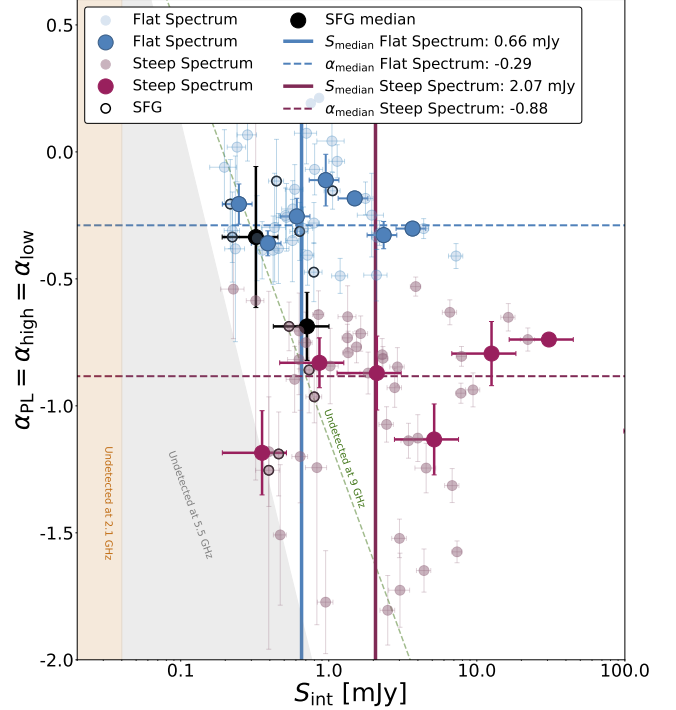


**Figure 10.** Distribution of the spectral indices of sources that show flat or steep spectral indices across the SHORES bands as a function of their 2.1 GHz flux density. The shaded regions mark the parameter space inaccessible due to sensitivity limits, indicating where a source, despite being detected at 2.1 GHz, would fall below the detection limit at the comparison frequencies (5.5/9 GHz) due to its spectral shape, resulting in an undefined spectral index.

Flat-spectrum sources, by contrast, cluster at the faint end and are more readily detected across our frequency range. Their distribution shows large scatter below  $\sim 2$  mJy but no clear trend with flux. No bright flat-spectrum AGN are found in the SHORES deep fields. Although this might indicate a real scarcity of such sources at these depths, we note that our spectral analysis relies on the availability of at least 3 photometric de-

tections, which could introduce selection effects against flat-spectrum sources with low-SNR in some bands. At these depths, flat indices likely arise from compact AGN cores or radio-quiet quasi-stellar objects (QSOs), possibly mixed with steeper star-forming components. Such composite systems have been reported in sub-mJy samples (e.g. Delvecchio et al. 2017; Smolčić et al. 2017; Whittam et al. 2022).

In summary, the faint population shows a non-monotonic spectral trend, with a flattening at intermediate fluxes and a steepening at the faint end. This likely reflects a mix of flat-spectrum AGN and star-forming galaxies. Broader spectral sampling, especially at sub-GHz frequencies, will help disentangle these contributions more robustly.

#### 4.2. Spectral behaviour in the 0.1-10 GHz regime

We reconstructed the SED across the radio domain for our sources by including the available radio ancillary data in the SED fit. In particular, we cross-matched our sources to identify counterparts in the Rapid ASKAP Continuum Survey (RACS, McConnell et al. 2020; Hale et al. 2021) and in the Galactic and Extra-Galactic All-Sky MWA Extended Survey (GLEAM-X, Ross et al. 2024).

RACS covers the whole sky at  $-90 < \delta < 49$  at  $\sim 887.5/943.5$  (RACS-low, McConnell et al. 2020), 1367.5 (RACS-mid, Hale et al. 2021) and 1655.5 MHz (RACS-high), reaching a sensitivity of  $\sim 0.25$  (RACS-low) and 0.2 mJy/beam (RACS-mid, high) with a resolution of  $\sim 15''$  (RACS-low),  $10''$  (RACS-mid) and  $8''$  (RACS-high). We find that 138 of our sources at  $\text{SNR} > 4.5$  have a RACS-low counterpart within a radius of  $15''$ , while 115 of the sources at  $\text{SNR} > 4.5$  have a RACS-mid counterpart and 143 in RACS-high.

We compared the RACS-mid and -high flux densities with those of our lowest sub-bands to confirm our findings (see Figure 11). Note that the systematic offset with RACS-low is expected. The flux density differences with RACS-low are fully consistent with the expected spectral behaviour between 900 MHz and our observing bands. When comparing RACS-low with our 1.3 GHz measurements, closer in frequency to 900 MHz, the discrepancy is significantly reduced. In contrast, the closer observing frequencies of RACS-mid (1367.5 MHz;  $\approx 10''$ ) and RACS-high (1655.5 MHz;  $\approx 8''$ ) yield a much tighter agreement with the SHORES flux scale.

GLEAM-X covers an area of  $1447 \text{ deg}^2$  around the South Galactic Pole region at  $-32.7 < \delta < -20.7$  with a median sensitivity 6.35 mJy/beam and a median resolution of  $45''$  (Ross et al. 2024; Hurley-Walker et al. 2022) with a broad spectral extension, spanning twenty fre-

quency bands in the range 72 to 231 MHz, complementing the spectral coverage towards the MHz side of the radio SED, where self-absorption processes take place. To match the statistic load of the GLEAM-X points in the fit with that of the higher frequencies, we average them in three broad band points. We cross-match our catalogue with GLEAM-X using a  $30''$  radius and find that 123 of our sources at  $\text{SNR} > 4.5$  have a GLEAM-X counterpart. Because our synthesized beam ( $\sim 4''$ ) is much smaller than the GLEAM-X beam ( $\sim 45''$ ), the main cross-matching concern is blending (multiple SHORES sources falling within a single GLEAM beam) rather than spurious matches. Using the confirmed sources per field (DEEP-1: 315; DEEP-2: 174) and assuming a circular GLEAM beam with  $r = \text{FWHM}/2 = 22.5''$ , we estimate  $\approx 5$  GLEAM beams in DEEP-1 and  $\approx 1-2$  in DEEP-2 to potentially contain  $\gtrsim 2$  SHORES sources. However, after a careful inspection during the cross-matching procedure, no such ambiguous cases were found.

As a result, 159 of our sources are detected in a minimum of 4 different radio bands at  $\text{SNR} > 4.5$ , that we used for the analysis described in the following subsections. Their radio spectral behaviour fitting resulted in the colour-colour plot presented in Figure 12 with the spectral indices distributions shown in Figure 13.

In Figure 12, we show the radio colour-colour diagram. Most sources follow a simple power-law spectrum: 44.2% are steep and 29.4% are flat, with no genuinely inverted also in this case. About 15.3% show pure peaked spectra and 1.2% (two sources) have curved but non-peaked spectra. Finally, 8.6% (14 sources) are fit by the retriggered model.

The resulting overall behaviour of the spectral index as a function of flux is the same as the one observed for the SHORES-only SED-fitting. In particular, there are 2.1 GHz-bright flat sources missed by the fitting based only on SHORES data, all but one because they are out of the mosaic area. The one in the mosaic might have a spectral change at higher frequencies that makes it invisible at 5.5-9 GHz.

The steep spectral indices distribution as a function of flux density has a turn-off (Figure 13) in this frequency range too, indicating the possibility of distinguishing emission due to nuclear activity or star formation. To help in this effort the combination with FIR data is necessary, as will be discussed in the next session.

## 5. RADIO TO FIR RELATIONS.

The FIRRC is a well-established empirical relationship observed in star-forming galaxies, linking their FIR and radio emissions (Helou et al. 1985; Delhaize et al.

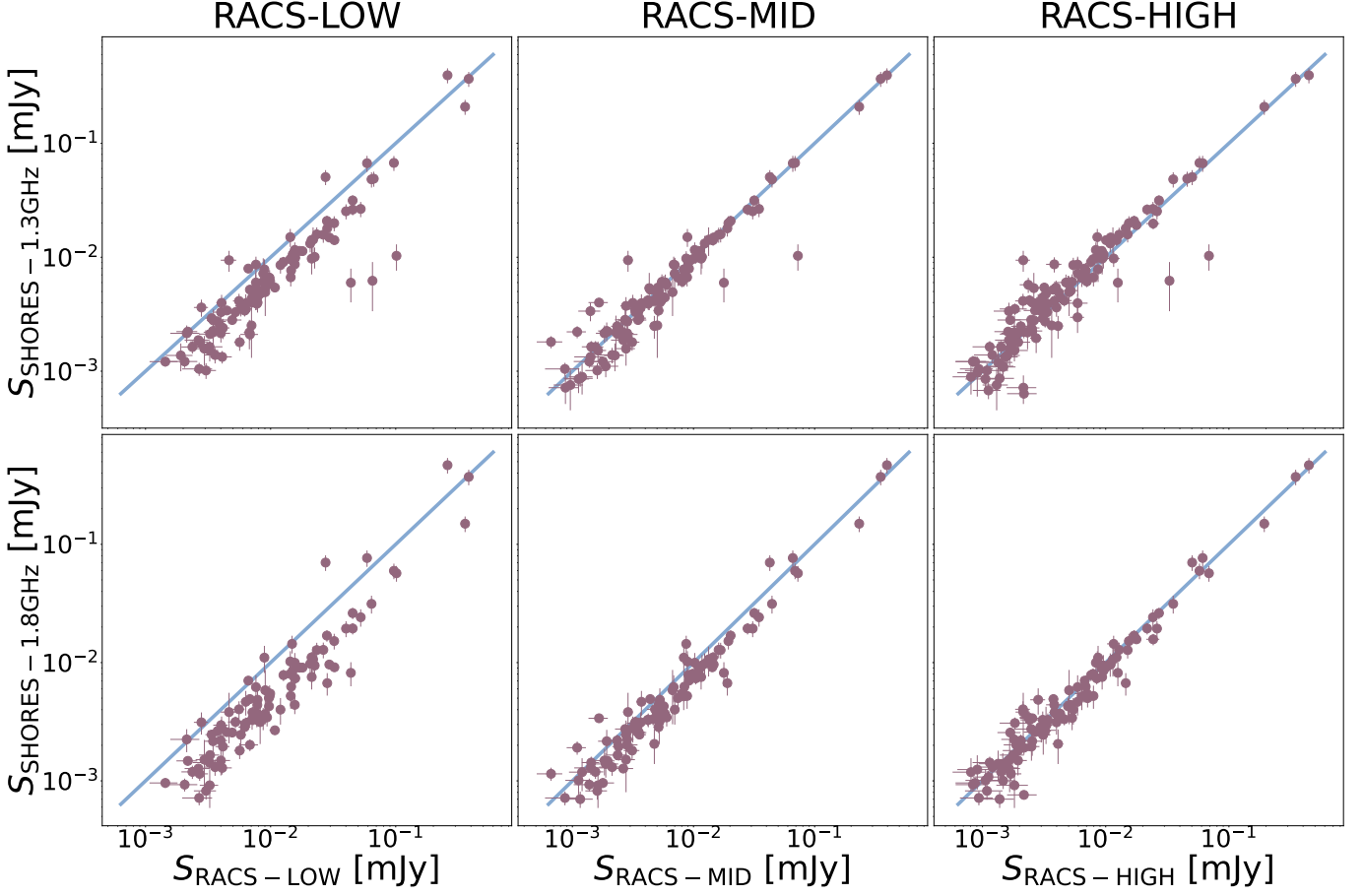


**Figure 11.** Comparison of SHORES 1.3 and 1.8 GHz sub-bands flux densities with RACS-mid, RACS-low and RACS-high ones.

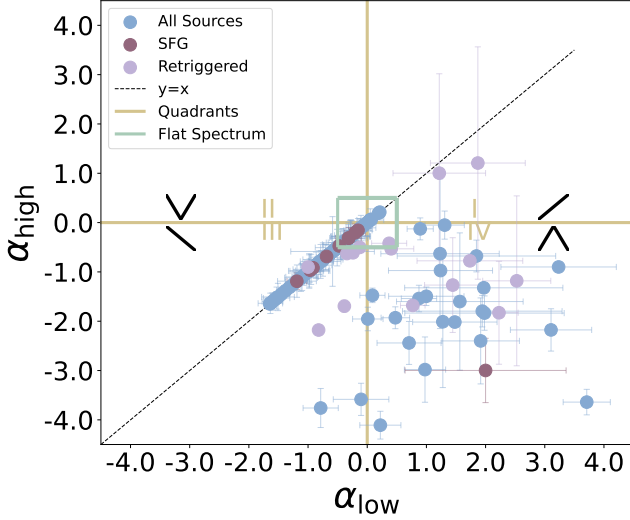


**Figure 12.** Radio colour-colour diagram of the sources in our sample, based on the spectral indices retrieved from the SED fitting across the 0.1-10 GHz regime.

1992; Yun et al. 2001; Ivison et al. 2010b; Jarvis et al. 2010; Smith et al. 2014; Giulietti et al. 2022). The

SHORES fields are selected in the H-ATLAS (Eales et al. 2010) survey to combine radio and FIR data.

We cross-matched the catalogues using a search radius of  $15''$ , comparable with the H-ATLAS resolution. Of our sources with a  $\text{SNR} > 4.5$ , 93 have an H-ATLAS counterpart with a detection in at least 3 different FIR bands: these are the sources considered in the following analysis of the FIRRC. In fact, this criterion ensures that we have reliable FIR measurements to estimate the FIR luminosity and to establish a robust correlation with radio data.

To quantify the FIRRC, we use the parameter  $q_{\text{FIR}}$ , which is defined as (Yun et al. 2001; Magnelli et al. 2015):

$$q_{\text{FIR}} = \log_{10} \left( \frac{L_{\text{FIR}}}{3.75 \times 10^{12} \text{W}} \right) - \log_{10} \left( \frac{L_{1.4 \text{ GHz}}}{\text{W Hz}^{-1}} \right) \quad (1)$$

where  $L_{\text{FIR}}$  is the total infrared luminosity (integrated over 8–1000  $\mu\text{m}$ ) and  $L_{1.4 \text{ GHz}}$  is the radio luminosity at 1.4 GHz. To calculate the luminosities based on the fluxes, we use the SPIRE redshift estimates reported in the H-ATLAS catalogue. In particular, the  $L_{\text{FIR}}$  is defined as



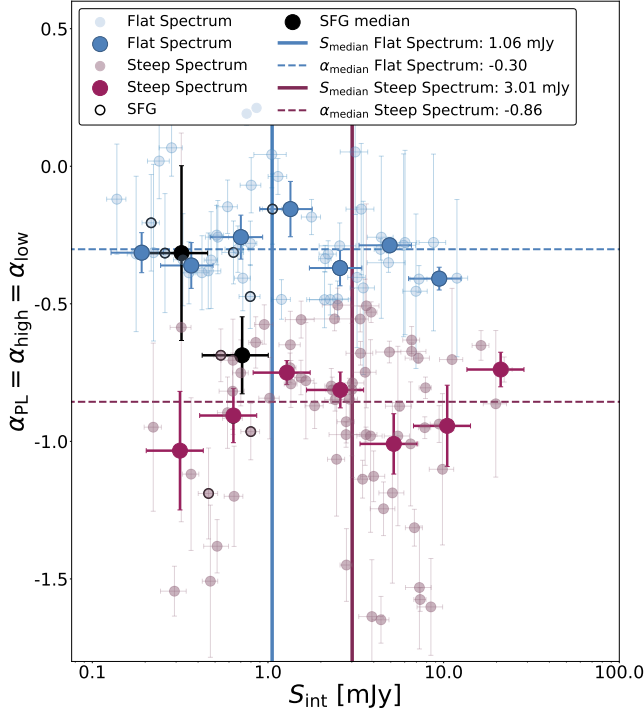


**Figure 13.** Distribution of the spectral indices of sources that show a flat or steep spectrum across the 0.1-10GHz radio regime as a function of the 2.1 GHz. We highlight with black empty circles the candidate SFGs based on the  $q_{\text{FIR}}$ .

$$L_{\text{FIR}} = \frac{4\pi D_L^2}{(1+z)} \int_{8\mu\text{m}}^{1000\mu\text{m}} S_{\nu,e} d\nu, \quad (2)$$

where  $D_L$  is the luminosity distance,  $z$  is the SPIRE redshift and  $S_{\nu,e}$  is the monochromatic flux density at a given infrared wavelength.

The rest-frame  $L_{1.4 \text{ GHz}}$  is computed as

$$L_{\nu,e} = \frac{4\pi D_L^2(z)}{(1+z)^{1+\alpha}} \left( \frac{\nu_e}{\nu_o} \right)^\alpha S_{\nu,o}, \quad (3)$$

where  $\alpha$  is the spectral index and the monochromatic radio flux density is  $S_\nu = \nu^\alpha$ .

Our median  $q_{\text{FIR}}$  is  $\sim 2.36$ , in full agreement with Ivison et al. (2010b):  $\sim 81\%$  of our analysed sources have a  $q_{\text{FIR}}$  within  $1\sigma$  from the value found by Ivison et al. (2010b) for SFGs. Condon et al. (2002) suggest  $q_{\text{FIR}} \sim 1.8$  as a threshold to distinguish between SFGs and AGN: only  $\sim 18.2\%$  of the considered sources are below this limit and should, thus, be considered AGN with FIR counterparts. In Figure 14 we show the relationship between  $q_{\text{FIR}}$  and redshift and radio luminosity. The existence of a trend of  $q_{\text{FIR}}$  with redshift remains a subject of considerable debate. In this work, we find that

$$q_{\text{FIR}} \sim 2.94(1+z)^{-0.22}, \quad (4)$$

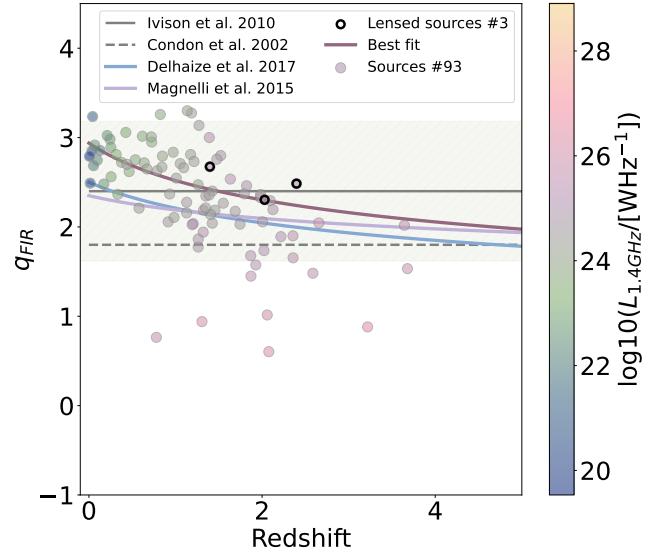


**Figure 14.** FIRRC  $q_{\text{FIR}}$  is shown as a function of redshift for 93 sources in our catalog, specifically those with at least three FIR photometric points, including 3 candidate lensed galaxies (black circles). The green shaded area represents the  $1\sigma$  dispersion around the value indicated by Ivison et al. (2010b) for SFGs. The colour bar represent the 1.4 GHz luminosity and the 500  $\mu\text{m}$  flux, respectively. The fractional uncertainty on the SPIRE photometric redshift amounts to  $\Delta z/(1+z) \approx 28\%$ .

i.e. a mild dependency on the redshift. We compare our results with Condon et al. (2002), Ivison et al. (2010b), Magnelli et al. (2015) and Delhaize et al. (2017). Magnelli et al. (2015) analysed a mass-selected sample of star-forming galaxies up to a redshift of approximately 2, and observed a marginal evolution characterized by the relation  $q_{\text{FIR}}(z) = (2.35 \pm 0.08)(1+z)^{-0.12 \pm 0.04}$ . Comparable findings were achieved by Delhaize et al. (2017) using a radio-selected sample of star-forming galaxies extending up to a redshift of approximately 6, with the relation  $q_{\text{FIR}}(z) = (2.52 \pm 0.03)(1+z)^{-0.21 \pm 0.01}$ .

In Figure 13, we show the spectral index distribution of the 19 sources that have both H-ATLAS and radio ancillary counterparts, to compare FIR and radio spectral behaviour. Of these, 10 have  $q_{\text{FIR}} \geq 1.69$ , i.e. the  $1\sigma$  lower bound of the Ivison et al. (2010b) FIR-radio relation for star-forming galaxies. In these objects, the emission is expected to be dominated by SF, the median spectral index is  $-0.6 \pm 0.1$ , in agreement with expectations for SFGs, as predicted by models of synchrotron emission from supernovae remnants (e.g. Condon et al. 1992; Murphy et al. 2009) and confirmed in statistical studies of FIR-selected SFGs (e.g. Delhaize et al. 2017; Magnelli et al. 2015).

However, we note that some of the power-law radio sources without FIR counterparts may in fact be SFGs,

undetected in FIR. The H-ATLAS survey is limited by instrumental confusion noise, particularly at 250–500  $\mu\text{m}$ , where the typical confusion limit is  $\sim 6\text{--}7$  mJy (e.g. Nguyen et al. 2010; Valiante et al. 2016). As a result, faint FIR emission from high-redshift SFGs may go undetected even when their radio counterparts are observable in deep maps. The spectral index distribution of these radio-only sources, peaking around  $\alpha \sim -0.6$ , is consistent with typical values expected for radio jets, but also of SFGs. This finding suggests that these sources could indeed be jets without any FIR counterpart, but yet a fraction of them could be composed by dust-obscured star-forming galaxies at  $z \gtrsim 1.5\text{--}2$ , falling below the Herschel detection limit.

Unfortunately, since our redshift estimates come solely from the H-ATLAS catalogue, we cannot meaningfully assess whether the *radio-detected but FIR-undetected* sources could exhibit a  $q_{\text{FIR}}$  value consistent with star-forming emission: without FIR photometry, there is no redshift estimate, and  $q_{\text{FIR}}$  cannot be evaluated.

However, we can perform a complementary and more robust test on the opposite class of objects: *H-ATLAS sources with FIR detections (and therefore photometric redshifts) but without radio counterparts*. For these galaxies, we used their FIR luminosities together with the adopted  $q_{\text{FIR}}(z)$  relation to predict the corresponding radio luminosities and, from these, the expected 2.1-GHz flux densities under the assumption that they are star-forming. This yields the predicted radio-flux distribution of the FIR-selected galaxies that SHORES should have detected if the survey had been deeper. As shown in Figure 15, the vast majority of these predicted fluxes lie below the 95% completeness limit of our radio observations and are significantly fainter than the fluxes of the FIR sources included in our catalogue.

This highlights the importance of combining deep radio and FIR observations when identifying and characterising faint SFGs. Nonetheless, caution is required when interpreting the spectral indices, as the observed radio emission may also be contaminated by non-stellar processes. These include galactic outflows or compact, low-luminosity AGN with no prominent FIR emission.

In conclusion, to disentangle these contributions and confirm the nature of these ambiguous sources, deeper observations in complementary wavebands, as millimetre (e.g. with ALMA) and X-ray data to build panchromatic SED fitting, are essential. Such multi-wavelength approaches can help break degeneracies between AGN and SFG emission mechanisms and improve the accuracy of FIRRC-based classifications, especially in the low-luminosity and high-redshift regimes.

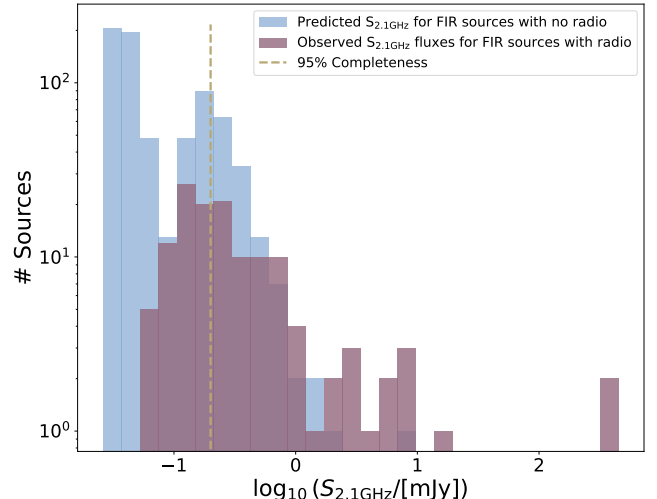


**Figure 15.** Observed 2.1 GHz flux densities for FIR-detected radio sources (purple) compared to the predicted 2.1 GHz fluxes of H-ATLAS sources with FIR detections but no radio counterparts (blue), computed from their FIR luminosities and photometric redshifts using the adopted  $q_{\text{FIR}}(z)$  relation. The vertical dashed line shows the 95% completeness limit. Most predicted fluxes lie below this threshold, naturally explaining their absence from the radio catalogue.

## 6. RADIO NUMBER COUNTS

We finally estimated the differential radio number counts for the SHORES deep fields (Figure 16 and Table 3-4) at 2.1 and 5.5 GHz.

Combining the source counts of the current paper with those of SHORES-I, we show how the SHORES survey, thanks to the combination of wide-area shallow fields and small-area deep fields, successfully recovers the bright and faint 2.1 GHz radio number counts down to flux densities of a few tens of  $\mu\text{Jy}$ , with comparable significance. The faintest bins are dominated by SFGs and possibly radio-quiet AGN, in line with what is expected from both empirical studies (e.g. Smolčić et al. 2017) and theoretical predictions (e.g. Mancuso et al. 2017). It is worth noting that the selection of SFGs is based on the  $q_{\text{FIR}}$  parameter, which could be estimated only for sources with at least three FIR detections. As a result, additional sources potentially contributing to the SFG number counts in the faint-end may be missed due to the sensitivity limits of H-ATLAS. Our observed number counts for fiducial SFGs qualitatively appear to follow the trend predicted for radio-quiet AGN in the evolutionary model by Mancuso et al. (2017). Considering the limited availability of FIR counterparts due to *Herschel*'s resolution and depth, along with incomplete radio photometric sampling for the faintest sources, we cautiously note that a fraction of sub-mJy sources classified as SFGs may host radio-

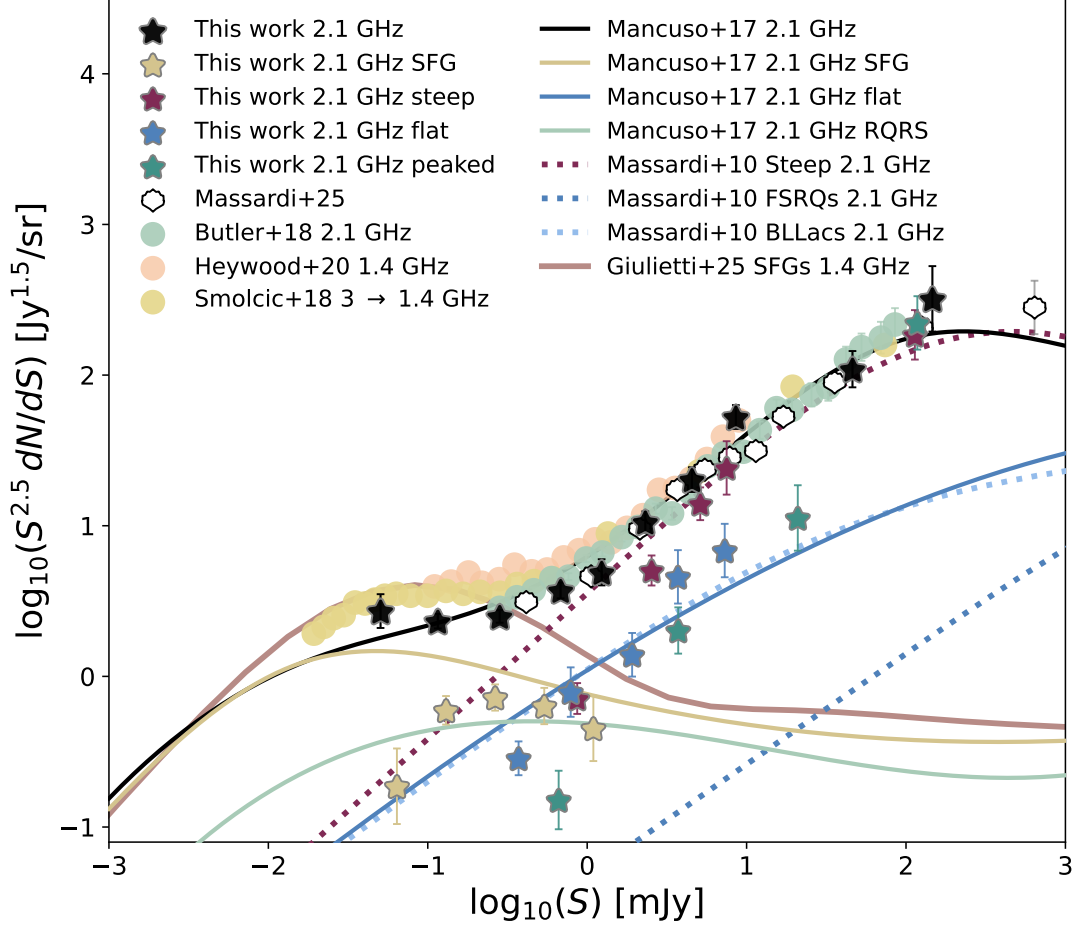


**Figure 16.** Euclidean differential source counts at 2.1 GHz of the two deep fields. For comparison we added recent estimates by SHORES-I, Butler et al. (2018), Heywood et al. (2020) and Smolčić et al. (2017) and the models by Massardi et al. (2010), Mancuso et al. (2017) and Giulietti et al. (2025). We highlight the differential number counts for the fiducial candidate star-forming galaxies with golden stars and the sources classified as steep (burgundy), flat (light blue) and peaked (green).

Intervals mJy	Bin Centers mJy	$N$	$S_{2.1\text{GHz}}^{2.5} dN/dS$ $\text{Jy}^{1.5}\text{sr}^{-1}$
0.026 - 0.076	0.051	15	$2.7 \pm 0.7$
0.076 - 0.156	0.116	81	$2.3 \pm 0.3$
0.156 - 0.410	0.283	109	$2.5 \pm 0.2$
0.410 - 0.953	0.681	68	$3.7 \pm 0.5$
0.953 - 1.512	1.232	25	$5.0 \pm 1.9$
1.511 - 3.118	2.315	38	$10.6 \pm 1.7$
3.118 - 5.958	4.538	28	$20.2 \pm 3.8$
5.958 - 11.160	8.559	30	$52.7 \pm 9.6$
11.160 - 81.160	46.160	13	$109.4 \pm 30.4$
81.160 - 211.600	146.381	4	$320.7 \pm 160.4$

**Table 3.** Differential Euclidean source counts at 2.1 GHz.

quiet AGN. The observed turnover in the differential counts below  $\sim 1$  mJy matches the well-known transition in source populations (see e.g. De Zotti et al. 2010; Massardi et al. 2010), and our measurements help fill

Intervals mJy	Bin Centers mJy	$N$	$S_{2.1\text{GHz}}^{2.5} dN/dS$ $\text{Jy}^{1.5}\text{sr}^{-1}$
0.042 - 0.086	0.064	3	$0.2 \pm 0.1$
0.086 - 0.175	0.130	21	$0.6 \pm 0.1$
0.174 - 0.355	0.265	25	$0.7 \pm 0.1$
0.355 - 0.721	0.538	13	$0.6 \pm 0.2$
0.721 - 1.466	1.093	4	$0.5 \pm 0.2$

**Table 4.** Differential Euclidean source counts 2.1 GHz for the fiducial SFGs.

the observational gap in the range 0.05–0.2 mJy where previous surveys often suffer from incompleteness.

We also compared our number counts with other deep surveys such as VLA-COSMOS (e.g. Smolčić et al. 2017) and MIGHTEE (Heywood et al. 2022), finding consistent trends. By leveraging matches with multi-wavelength ancillary data, we attempted a statistical separation of SFGs and AGNs with different spectral

properties at low flux densities—bearing in mind the limitations due to incomplete FIR coverage and multi-frequency detection thresholds. While this spectral and multi-band decomposition does not allow us to disentangle the different evolutionary models, the resulting distributions appear qualitatively consistent with the expected behaviour of SFGs and radio-quiet AGN on the one hand (e.g. Mancuso et al. 2017), and of radio-loud AGN on the other (e.g. Bonato et al. 2021). Within the limits of the current completeness, this broad consistency supports the tentative use of such classifications to statistically explore the nature of the faint radio population.

## 7. SUMMARY AND PERSPECTIVES

We presented the building and analysis of the catalogue of the SHORES survey deep fields at 2.1 GHz, and of their follow-up at 5.5 and 9.0 GHz. The catalogue at 2.1 GHz is based on source extraction from two  $\sim 1.2 \text{ deg}^2$  mosaics (Deep 1 and Deep 2), selected for their rich ancillary coverage and lack of bright contaminating sources. The Deep 1 mosaic reaches an rms of  $\sigma \simeq 9 \mu\text{Jy}/\text{beam}$ , while Deep 2 reaches  $\sigma \simeq 18 \mu\text{Jy}/\text{beam}$  over the same area. Thus, the SHORES deep survey covers  $2.4 \text{ deg}^2$  with a mean rms sensitivity of  $\sim 13.5 \mu\text{Jy}/\text{beam}$ . The extracted catalogue is 95% complete above  $183 \mu\text{Jy}$  ( $4.5\sigma$  in the shallower field) and 85% reliable above the adopted  $4.5\sigma$  threshold. The follow-up in mosaic mode of the inner  $0.5 \times 0.5 \text{ deg}^2$  of each field provided a catalogue of 101 counterparts at 5.5 GHz and 33 at 9.0 GHz.

The analysis of the spectral behaviour in the observed frequency range pointed out that to such sensitivity levels the flat-steep spectra sources dominates the population, while peaked spectra remain a 15.7% fraction, indicating the relevant role that SF plays over jetted AGN components. The combination with lower frequency radio and FIR ancillary data stressed the importance of a multi-wavelength analysis for  $< 1 \mu\text{Jy}$  radio sources classification. About 18.7% of our sources have a counterpart in H-ATLAS, mostly with  $\text{FIRRC} > 1.7$ , stressing the relevance of SF over nuclear activity in such sources. We identified for them a trend of  $\text{FIRRC}$  with redshift and an average spectral index over the whole radio domain  $\alpha \sim -0.6 \pm 0.1$ .

We finally presented the source counts at 2.1 for our sample, including in the former the separation between SFG and AGN-dominated sources as made possible by our attempted classification. Our findings are in good agreement with previous datasets and with in-situ theoretical models for galaxy formation (Mancuso et al. 2017). Our findings highlight the importance of deep, multi-frequency radio surveys over well-characterised extragalactic fields and demonstrate the value of combining radio and FIR data for disentangling source populations. In this context, SHORES represents a key preparatory step for the SKA era, bridging the observational gap between current large-area shallow surveys and pencil-beam ultra-deep fields.

We acknowledge Q. D’Amato for his contributions in the early stages of the SHORES survey. M. Behiri acknowledges the support given by L. Capuano, A. Traina and L. Leuzzi and the 06:39 Frecciarossa train from Trieste Centrale to Bologna Centrale. This work was partially funded from the projects: INAF GO-GTO Normal 2023 funding scheme with the project “Serendipitous H-ATLAS-fields Observations of Radio Extragalactic Sources (SHORES)” ; INAF Large Grant 2022 project “MeerKAT and LOFAR Team up: a Unique Radio Window on Galaxy/AGN co-Evolution”; INAF Large GO 2024 project “MeerKAT and Euclid Team up: Exploring the galaxy-halo connection at cosmic noon”; “Data Science methods for MultiMessenger Astrophysics & Multi-Survey Cosmology”, funded by the Italian Ministry of University and Research, Programmazione triennale 2021/2023 (DM n.2503 dd. 9 December 2019), Programma Congiunto Scuole; Italian Research Center on High Performance Computing Big Data and Quantum Computing (ICSC), project funded by European Union - NextGenerationEU - and National Recovery and Resilience Plan (NRRP) - Mission 4 Component 2 within the activities of Spoke 3 (Astrophysics and Cosmos Observations); European Union - NextGenerationEU under the PRIN MUR 2022 project n.20224JR28W “Charting unexplored avenues in Dark Matter”.

*Facilities:* ATCA

*Software:* RADIOSED (Kerrison et al. 2024) BLOBCAT (Hales et al. 2012) MIRIAD (Sault et al. 1995) PySE (Carbone et al. 2018) WSCLEAN (Oftringa et al. 2014b)

## REFERENCES

Behiri, M., Talia, M., Cimatti, A., et al. 2023, ApJ, 957, 63, doi: [10.3847/1538-4357/acf616](https://doi.org/10.3847/1538-4357/acf616)

Bell, E. F. 2003, ApJ, 586, 794, doi: [10.1086/367829](https://doi.org/10.1086/367829)



- Best, P. N., Kondapally, R., Williams, W. L., et al. 2023, *MNRAS*, 523, 1729, doi: [10.1093/mnras/stad1308](https://doi.org/10.1093/mnras/stad1308)
- Blandford, R. D., & Znajek, R. L. 1977, *Monthly Notices of the Royal Astronomical Society*, 179, 433, doi: [10.1093/mnras/179.3.433](https://doi.org/10.1093/mnras/179.3.433)
- Bonato, M., Prandoni, I., De Zotti, G., et al. 2021, *MNRAS*, 500, 22, doi: [10.1093/mnras/staa3218](https://doi.org/10.1093/mnras/staa3218)
- Butler, A., Huynh, M., Delhaize, J., et al. 2018, *A&A*, 620, A3, doi: [10.1051/0004-6361/201630129](https://doi.org/10.1051/0004-6361/201630129)
- Carbone, D., Garsden, H., Spreeuw, H., et al. 2018, *Astronomy and Computing*, 23, 92, doi: [10.1016/j.ascom.2018.02.003](https://doi.org/10.1016/j.ascom.2018.02.003)
- Condon, J. J., Cotton, W. D., & Broderick, J. J. 2002, *AJ*, 124, 675, doi: [10.1086/341650](https://doi.org/10.1086/341650)
- Condon, J. J., et al. 1992, *ARA&A*, 30, 575
- De Zotti, G., Massardi, M., Negrello, M., & Wall, J. 2010, *A&A Rv*, 18, 1, doi: [10.1007/s00159-009-0026-0](https://doi.org/10.1007/s00159-009-0026-0)
- Delhaize, J., et al. 1992, *A&A*, 602, A4
- Delhaize, J., Smolčić, V., Delvecchio, I., et al. 2017, *A&A*, 602, A4, doi: [10.1051/0004-6361/201629430](https://doi.org/10.1051/0004-6361/201629430)
- Delvecchio, I., Smolčić, V., Zamorani, G., et al. 2017, *A&A*, 602, A3, doi: [10.1051/0004-6361/201629367](https://doi.org/10.1051/0004-6361/201629367)
- Eales, S., Dunne, L., Clements, D., et al. 2010, *PASP*, 122, 499, doi: [10.1086/653086](https://doi.org/10.1086/653086)
- Franzen, T. M. O., Banfield, J. K., Hales, C. A., et al. 2015, *MNRAS*, 453, 4020, doi: [10.1093/mnras/stv1866](https://doi.org/10.1093/mnras/stv1866)
- Galluzzi, V., Massardi, M., Bonaldi, A., et al. 2017, *MNRAS*, 465, 4085, doi: [10.1093/mnras/stw3017](https://doi.org/10.1093/mnras/stw3017)
- Gentile, F., Talia, M., Behiri, M., et al. 2024, *ApJ*, 962, 26, doi: [10.3847/1538-4357/ad1519](https://doi.org/10.3847/1538-4357/ad1519)
- Giulietti, A., et al. 2022, *MNRAS*, 511, 1408
- Giulietti, M., Prandoni, I., Bonato, M., et al. 2025, *A&A*, 697, A81, doi: [10.1051/0004-6361/202453331](https://doi.org/10.1051/0004-6361/202453331)
- Hale, C. L., McConnell, D., Thomson, A. J. M., et al. 2021, *PASA*, 38, e058, doi: [10.1017/pasa.2021.47](https://doi.org/10.1017/pasa.2021.47)
- Hale, C. L., Whittam, I. H., Jarvis, M. J., et al. 2023, *MNRAS*, 520, 2668, doi: [10.1093/mnras/stac3320](https://doi.org/10.1093/mnras/stac3320)
- Hales, C. A., Murphy, T., Curran, J. R., et al. 2012, *MNRAS*, 425, 979, doi: [10.1111/j.1365-2966.2012.21373.x](https://doi.org/10.1111/j.1365-2966.2012.21373.x)
- Hancock, P. J., Trott, C. M., & Hurley-Walker, N. 2018, *PASA*, 35, e011, doi: [10.1017/pasa.2018.3](https://doi.org/10.1017/pasa.2018.3)
- Helou, G., Soifer, B. T., & Rowan-Robinson, M. 1985, *ApJL*, 298, L7, doi: [10.1086/184556](https://doi.org/10.1086/184556)
- Heywood, I., Hale, C. L., Jarvis, M. J., et al. 2020, *MNRAS*, 496, 3469, doi: [10.1093/mnras/staa1770](https://doi.org/10.1093/mnras/staa1770)
- Heywood, I., Jarvis, M. J., Hale, C. L., et al. 2022, *MNRAS*, 509, 2150, doi: [10.1093/mnras/stab3021](https://doi.org/10.1093/mnras/stab3021)
- Hurley-Walker, N., Galvin, T. J., Duchesne, S. W., et al. 2022, *PASA*, 39, e035, doi: [10.1017/pasa.2022.17](https://doi.org/10.1017/pasa.2022.17)
- Ivison, R. J., Swinbank, A. M., Swinyard, B., et al. 2010a, *A&A*, 518, L35, doi: [10.1051/0004-6361/201014548](https://doi.org/10.1051/0004-6361/201014548)
- Ivison, R. J., Magnelli, B., Ibar, E., et al. 2010b, *A&A*, 518, L31, doi: [10.1051/0004-6361/201014552](https://doi.org/10.1051/0004-6361/201014552)
- Jarvis, M., Taylor, R., Agudo, I., et al. 2016, in *MeerKAT Science: On the Pathway to the SKA*, 6, doi: [10.22323/1.277.0006](https://doi.org/10.22323/1.277.0006)
- Jarvis, M. J., Smith, D. J. B., Bonfield, D. G., et al. 2010, *Monthly Notices of the Royal Astronomical Society*, 409, 92, doi: [10.1111/j.1365-2966.2010.17772.x](https://doi.org/10.1111/j.1365-2966.2010.17772.x)
- Kerrison, E. F., Allison, J. R., Moss, V. A., Sadler, E. M., & Rees, G. A. 2024, *MNRAS*, 533, 4248, doi: [10.1093/mnras/stae1796](https://doi.org/10.1093/mnras/stae1796)
- Magnelli, B., et al. 2015, *A&A*, 573, A45
- Mancuso, C., et al. 2017, *ApJ*, 842, 95
- Massardi, M., Behiri, M., Galluzzi, V., et al. 2025, *PASP*, 137, 014101, doi: [10.1088/1538-3873/ada826](https://doi.org/10.1088/1538-3873/ada826)
- Massardi, M., Bonaldi, A., Negrello, M., et al. 2010, *MNRAS*, 404, 532, doi: [10.1111/j.1365-2966.2010.16305.x](https://doi.org/10.1111/j.1365-2966.2010.16305.x)
- Massardi, M., Ekers, R. D., Murphy, T., et al. 2011, *MNRAS*, 412, 318, doi: [10.1111/j.1365-2966.2010.17917.x](https://doi.org/10.1111/j.1365-2966.2010.17917.x)
- McConnell, D., Hale, C. L., Lenc, E., et al. 2020, *PASA*, 37, e048, doi: [10.1017/pasa.2020.41](https://doi.org/10.1017/pasa.2020.41)
- Murphy, E. J., et al. 2009, *ApJ*, 706, 482
- Negrello, M., Amber, S., Amvrosiadis, A., et al. 2017, *MNRAS*, 465, 3558, doi: [10.1093/mnras/stw2911](https://doi.org/10.1093/mnras/stw2911)
- Nguyen, H. T., Schulz, B., Levenson, L., et al. 2010, *A&A*, 518, L5, doi: [10.1051/0004-6361/201014680](https://doi.org/10.1051/0004-6361/201014680)
- Norris, R. P., Marvil, J., Collier, J. D., et al. 2021, *PASA*, 38, e046, doi: [10.1017/pasa.2021.42](https://doi.org/10.1017/pasa.2021.42)
- Offringa, A. R., McKinley, B., Hurley-Walker, N., et al. 2014a, *MNRAS*, 444, 606, doi: [10.1093/mnras/stu1368](https://doi.org/10.1093/mnras/stu1368)
- . 2014b, *MNRAS*, 444, 606, doi: [10.1093/mnras/stu1368](https://doi.org/10.1093/mnras/stu1368)
- Planck Collaboration, Aghanim, N., Akrami, Y., et al. 2020, *A&A*, 641, A1, doi: [10.1051/0004-6361/201833880](https://doi.org/10.1051/0004-6361/201833880)
- Prandoni, I., Parma, P., Wieringa, M. H., et al. 2006, *A&A*, 457, 517, doi: [10.1051/0004-6361:20054273](https://doi.org/10.1051/0004-6361:20054273)
- Ross, K., Hurley-Walker, N., Galvin, T. J., et al. 2024, *PASA*, 41, e054, doi: [10.1017/pasa.2024.57](https://doi.org/10.1017/pasa.2024.57)
- Sargent, M. T., Schinnerer, E., Murphy, E., et al. 2010, *ApJS*, 186, 341, doi: [10.1088/0067-0049/186/2/341](https://doi.org/10.1088/0067-0049/186/2/341)
- Sault, R. J., Teuben, P. J., & Wright, M. C. H. 1995, in *Astronomical Society of the Pacific Conference Series*, Vol. 77, *Astronomical Data Analysis Software and Systems IV*, ed. R. A. Shaw, H. E. Payne, & J. J. E. Hayes, 433, doi: [10.48550/arXiv.astro-ph/0612759](https://doi.org/10.48550/arXiv.astro-ph/0612759)
- Smith, D. J. B., Jarvis, M. J., Hardcastle, M. J., et al. 2014, *Monthly Notices of the Royal Astronomical Society*, 445, 2232, doi: [10.1093/mnras/stu1830](https://doi.org/10.1093/mnras/stu1830)

- Smith, D. J. B., Haskell, P., Gürkan, G., et al. 2021, A&A, 648, A6, doi: [10.1051/0004-6361/202039343](https://doi.org/10.1051/0004-6361/202039343)
- Smolčić, V., Delvecchio, I., Zamorani, G., et al. 2017, A&A, 602, A2, doi: [10.1051/0004-6361/201630223](https://doi.org/10.1051/0004-6361/201630223)
- Talia, M., Cimatti, A., Giulietti, M., et al. 2021, ApJ, 909, 23, doi: [10.3847/1538-4357/abd6e3](https://doi.org/10.3847/1538-4357/abd6e3)
- Valiante, E., Smith, M. W. L., Eales, S., et al. 2016, MNRAS, 462, 3146, doi: [10.1093/mnras/stw1806](https://doi.org/10.1093/mnras/stw1806)
- Whittam, I. H., Jarvis, M. J., Hale, C. L., et al. 2022, MNRAS, 516, 245, doi: [10.1093/mnras/stac2140](https://doi.org/10.1093/mnras/stac2140)
- Yun, M. S., Reddy, N. A., & Condon, J. J. 2001, ApJ, 554, 803, doi: [10.1086/323145](https://doi.org/10.1086/323145)